On the Impact of Cadmium Sulfide Layer Thickness on Kesterite Photodetector Performance

Zeiske, Stefan; Kaiser, Christina; Sandberg, Oskar J.; Ericson, Tove; Meredith, Paul; Platzer-Björkman, Charlotte; Armin, Ardalan

Link to publication

On the Impact of Cadmium Sulfide Layer Thickness on Kesterite Photodetector Performance

Stefan Zeiske,* Christina Kaiser, Oskar J. Sandberg, Tove Ericson, Paul Meredith, Charlotte Platzer-Björkman,* and Ardalan Armin*

Kesterites are currently viewed as one of the most promising candidates for earth abundant and benign elements to substitute critical raw materials in photovoltaic technologies and may also be suitable for low-noise, room-temperature, self-powered photodetectors. However, while the impact of buffer layers on kesterite solar cell efficiency has been an active area of investigation, links between photodetector performance and intermediate layers are yet to be addressed. Herein, the impact of cadmium sulfide buffer layers on the performance of kesterite (Cu_2ZnSnS_4) photodetectors is probed. Specifically, the effect of buffer layer thickness on various photodetector performance metrices is clarified, including noise current, spectral responsivity, noise equivalent power, frequency response, and specific detectivity. Devices with a 100 nm cadmium sulfide layer perform the best, achieving a linear dynamic range of 180 dB and frequency responses in the range of tens of kHz. The key loss mechanisms are identified, and it is found that the photodetector performance to be primarily limited by shunt resistance-induced thermal noise and defect-induced nonradiative losses. Furthermore, we estimate the upper radiative limit of specific detectivity to be approximately 10^{19} Jones. Our results highlight the potential of kesterites to be used as an interesting earth abundant candidate for photodetection applications.

S. Zeiske, C. Kaiser, O. J. Sandberg, P. Meredith, A. Armin
Sustainable Advanced Materials (Sêr-SAM)
Department of Physics
Swansea University
Singleton Park, Swansea SA2 8PP, UK
E-mail: stefan.zeiske@swansea.ac.uk; ardalan.armin@swansea.ac.uk

T. Ericson, C. Platzer-Björkman
Division for Solar Cell Technology
Department of Materials Science and Engineering
Uppsala University
75103 Uppsala, Sweden
E-mail: charlotte.platzer@uu.se

T. Ericson
Department of Chemistry-Ångström
Uppsala University
75120 Uppsala, Sweden

1. Introduction

Extensive research into the class of critical raw material (CRM)-free, thin-film photovoltaic (PV) technology has been conducted over the past decade aiming to (partially) substitute CRM elements, such as indium (In), tellurium (Te), or gallium (Ga), with earth abundant, benign elements to build the basis for an environment-friendly, cost-efficient PV technology. Among the CRM-free PV materials is the class of kesterites, i.e., Cu_2ZnSnS_4 (CZTS) and $Cu_2ZnSnSe_4$ (CZTSe). Related alloys $Cu_2ZnSn(S,Se)_4$ and (CZTSSe) are currently viewed as one of the most promising CRM-free candidates for PV applications[1,2] due to their bandgap tuneability (between ≈ 1 and ≈ 1.5 eV depending on the sulfur (S)-to-selenium (Se) ratio),[3] intrinsic *p*-type conductivity,[4] and relatively high absorption coefficients ($\alpha \sim 10^4$ cm^{-1}).[5] These advantageous electro-optical properties make kesterites not only suitable for solar cell applications[6–8] but also for photocatalysis,[9,10] gas sensing,[11,12] and photodetection.[13] However, a closer look into the performance of kesterites in the different PV application sectors reveals that their efficiency is often still far below their CRM competitors. Here, large voltage deficits,[14,15] defect states,[16–18] narrow phase-stabilities, and interface recombination,[19] as well as nonideal device architectures, have been suggested as key issues limiting kesterite performance.

Kesterite solar cell research has been primarily focused on the optimization of the intermediate buffer layers—most commonly, zinc-tin oxide (ZTO), zinc oxysulfide (ZnOS), indium(III) sulfide (In$_2$S$_3$), and cadmium sulfide (CdS).[20,21] CdS is an *n*-type semiconductor with high photosensitivity in the visible (VIS).[22] By optimizing the CdS buffer layer, Gong et al. demonstrated low-temperature annealing to reduce the elemental demixing-induced interface recombination in CdS/CZTS heterojunctions, resulting in a power conversion efficiency of 13% for kesterite solar cells,[6] which was recently surpassed by Zhou and co-workers by regulating the CZTSSe phase evolution during selenization resulting in 13.8% power conversion efficiency devices.[23]

In contrast, research on kesterite-based photodetectors has been mainly focused on the kesterite bulk for response time optimization and spectral responsivity enhancement. As such, Singh

et al. found Na-doping-induced enhancements in "on-off" switching times for near-infrared (NIR) CZTS photodetectors.[24] In a follow-up work, Gour et al. demonstrated broad spectral response of rice-like nanostructured CZTS self-powered photodetectors for VIS and NIR wavelength regimes accompanied by detectivities of up to $\sim 4.5 \times 10^8$ Jones.[25] In 2017, reactive sputtering-grown CZTSSe thin-film photodetectors were shown to exhibit superior response times and increased detectivities of 3.5×10^9 Jones.[13] Furthermore, enhanced photocarrier transport in highly oriented CZTS/ZnO photodetectors was identified to be origin of increased photocurrent leading to high responsivities, fast rise and fall response times, as well as good photocurrent cycle response stability.[26] However, a complete characterization of photodetector performance and careful identification of efficiency-limiting factors in kesterite-based photodetectors have thus far been lacking in the literature. In particular, the link between CdS buffer layers and photodetector performance has yet to be established. Based on determined efficiency-loss channels and links between photodetector performance and device architecture, kesterite fabrication pathways could be improved in the future and performance efficiencies ultimately enhanced.

In this work, we investigate kesterite (Cu$_2$ZnSnS$_4$, CZTS) photodetectors with different thicknesses of CdS buffer layers. We characterize the kesterite photodetectors with regard to their main performance metrices, including specific detectivity (D^*), noise equivalent power (NEP), linear dynamic range (LDR), and frequency response. From current-versus-voltage curves and photovoltaic external quantum efficiency (EQE) measurements, we find the photodetector performances to be limited by high shunt currents and defect-induced nonradiative losses. Finally, we estimate the upper radiative limit of the specific detectivity to be approximately 10^{19} Jones—a value highlighting the potential of kesterites to be used as viable, CRM-free candidates for sustainable, environment-friendly photodetectors.

2. Results

A series of kesterite (Cu$_2$ZnSnS$_4$, CZTS) photodetectors with different cadmium sulfide (CdS) buffer layer thicknesses (d_{CdS}) of nominally 30, 50, and 100 nm were fabricated having the following device architecture: glass | Mo | CZTS (2 μm) | CdS (30–100 nm) | ZnO | ZnO:Al. In **Figure 1**, the corresponding responsivity, current–voltage, and noise–frequency characteristics are shown. Details of the device fabrication and the technical details related to the responsivity, current, and noise measurements are provided in Experimental Section. Figure 1a shows the experimentally determined responsivity ($R = dI/dL$, where I is the device photocurrent and L is the incident light power) of the three CZTS devices plotted as a function of wavelength, revealing a spectral response in the VIS between ~ 400 and ~ 850 nm. Maximum responsivities of approximately 0.31 AW^{-1} (30 nm; red solid line), 0.35 AW^{-1} (50 nm; blue solid line), and 0.30 AW^{-1} (100 nm; red solid line) were achieved at a probe wavelength of 680 nm (for the 30 and 50 nm CdS CZTS devices) and 700 nm (for the 100 nm CdS CZTS device); the bandgap was estimated to be $E_g \approx 1.4$ eV for all three CZTS devices.

Figure 1b shows the current versus applied voltage curves measured in the dark (solid lines) and under artificial 1 sun (AM1.5 G condition) illumination (dashed lines). The CZTS devices were found to exhibit short-circuit currents (I_{sc}) of 7.46, 8.46, and 6.72 mA and open-circuit voltages (V_{oc}) of 0.6, 0.61, and 0.62 V for a CdS thickness of 30, 50, and 100 nm, respectively. Based on the slopes of the dark current (I_D)–voltage (V) curves at zero bias, the shunt resistances were determined and found to be $R_{shunt} \approx 16$ kΩ (30 nm), $R_{shunt} \approx 7.5$ kΩ (50 nm), and $R_{shunt} \approx 21$ kΩ (100 nm). No correlation was observed between CdS buffer layer thickness and shunt resistance.

2.1. Noise Current

The noise current (I_{noise}) versus frequency (f) spectra in the dark of all three devices is displayed in Figure 1c at bias voltages ranging from -1 V (light color) to 0 V (black). The I_{noise}–f curves are characterized by i) a strong $1/f$ dependence in the low-frequency limit indicative of flicker noise, ii) I_{noise} peaks at multiples of 50 Hz as a result of humming noise, and iii) a continuous decrease in I_{noise} towards higher frequencies until it becomes (almost) frequency independent and free of hum noise. In the high-frequency limit of the measurement, I_{noise} decreases with increasing CdS buffer layer thickness. Furthermore, I_{noise} increases with higher reverse bias in all three CZTS devices—an observation often attributed to the presence of a shot-noise component (I_{shot}), which is related to the dark current I_D via

$$I_{shot} = \sqrt{2q\Delta f I_D} \tag{1}$$

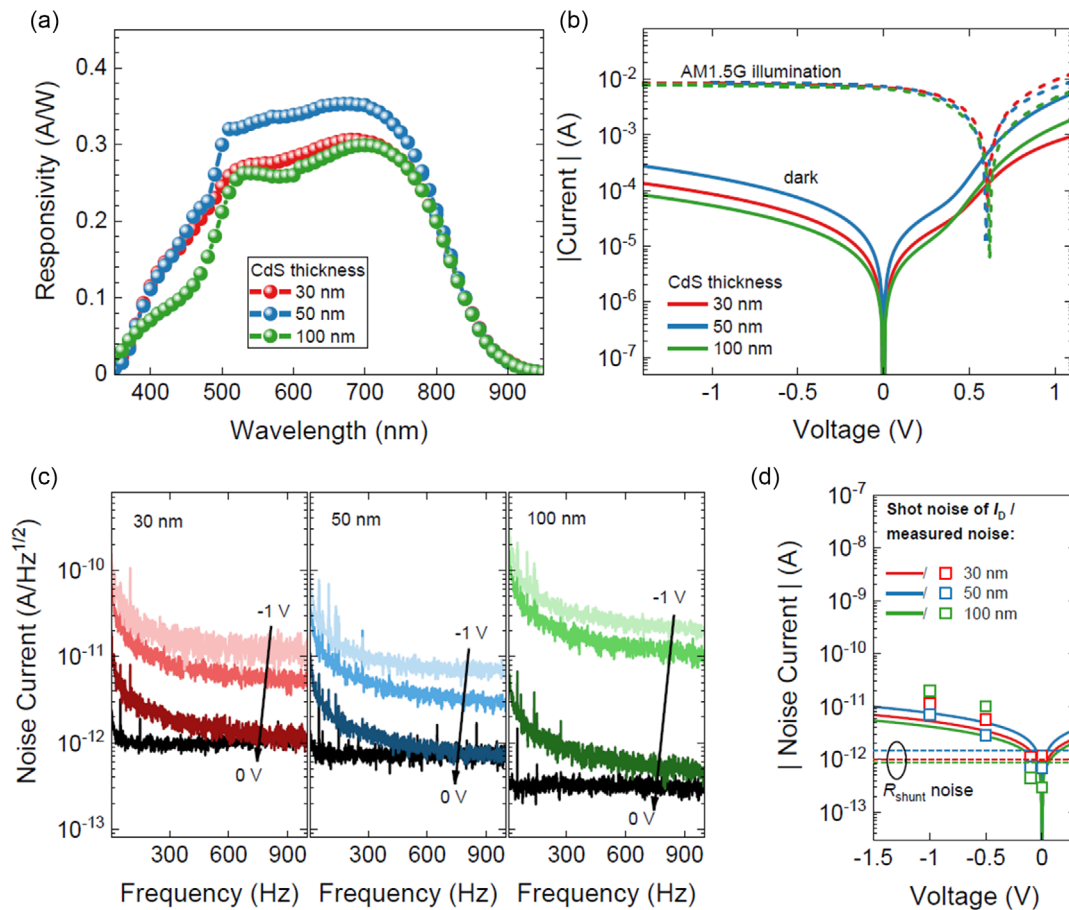where q is the elementary charge, and Δf is the electrical bandwidth. Figure 1d shows the calculated "would-be" I_{shot} based on I_D (solid line) and the measured I_{noise} (symbols) plotted as a function of voltage for an electrical bandwidth of 1 Hz. It can be seen that I_{shot} and I_{noise} are in good agreement with deviations less than one order of magnitude. For comparison, we included the expected (voltage independent) thermal noise current induced by the shunt resistances, calculated via $I_{thermal} = \sqrt{4k_B T\Delta f/R_{shunt}}$, where T is the temperature and k_B is the Boltzmann constant. $I_{thermal}$ for the three kesterite photodetectors with CdS buffer layer thickness of 30, 50, and 100 nm were found to be 1.01×10^{-12}, 1.48×10^{-12}, and 8.82×10^{-13} A, respectively, as indicated by horizontal dashed lines in Figure 1d.

2.2. Noise Equivalent Power

The specific detectivity (D^*) represents the signal-to-noise ratio (SNR) generated by the photodetector at a given incident light power (1 W). D^* is one of the main performance metrics of a photodetector and is connected to the spectral responsivity and noise current via

$$D_R^* = \frac{R\sqrt{A\Delta f}}{I_{noise}} \tag{2}$$

where A denotes the active area. Here, the subscript R denotes that the detectivity is calculated from responsivity, R. **Figure 2**a

**ADVANCED
SCIENCE NEWS**

www.advancedsciencenews.com

**ADVANCED
PHOTONICS
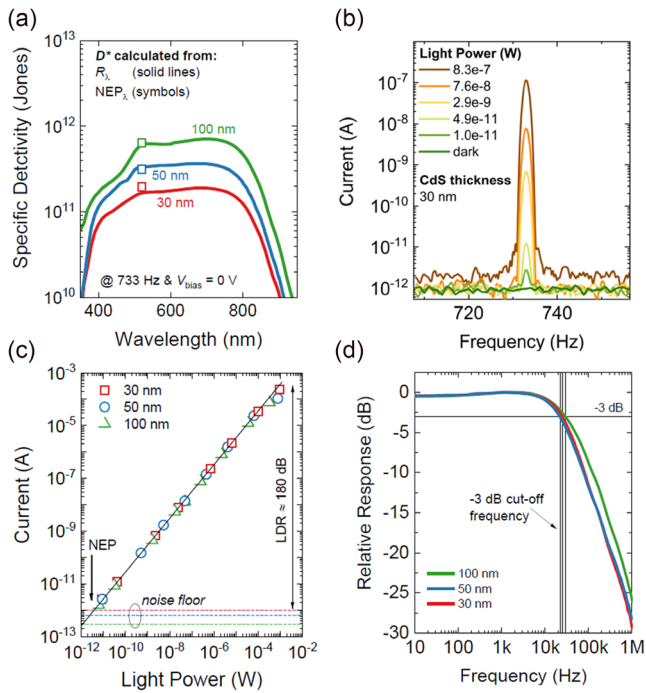RESEARCH**
Open Access

www.adpr-journal.com

Figure 1. a) Responsivity plotted as a function of wavelength and compared for three CZTS devices with different CdS buffer layer thicknesses: 30, 50, and 100 nm. b) Current versus voltage characteristics of the same devices measured in the dark (solid lines) and under artificial 1 sun (AM1.5 G condition) illumination. c) Noise current plotted as a function of frequency for all three kesterite photodetectors and compared at different applied reverse bias voltages between −1 V (light color) and 0 V (black). d) Calculated shot noise (symbols), thermal noise (horizontal, dashed line), and measured noise current (line) with an electrical bandwidth of 1 Hz plotted as a function of voltage.

shows D_R^*, as determined from the measured responsivity in accordance with Equation (2) (solid lines; for $\Delta f = 1$ Hz), plotted as a function of wavelength. Here, a maximum D_R^* of 1.91×10^{11} Jones (30 nm), 3.66×10^{11} Jones (50 nm), and 7.12×10^{11} Jones (100 nm) were obtained at a wavelength of 680 nm (30 and 50 nm CdS CZTS device) and 700 nm (100 nm CdS CZTS device).

The (wavelength-dependent) noise equivalent power (NEP$_\lambda$) was determined for the three CZTS photodetectors by probing the corresponding photocurrent as a function of light power sensitively over a broad range of light intensities. To this end, the probe light of a 520 nm laser diode was modulated at 733 Hz (avoiding $1/f$ flicker and hum noise) and gradually attenuated until the photocurrent coincided with the corresponding noise current obtained in the dark (see Figure 1c; noise current at zero applied bias voltage and $f = 733$ Hz). Further details are provided in the Experimental Section. In Figure 2b, the photocurrent spectra of the CZTS device with 30 nm CdS buffer layer are plotted against the frequency and compared at different incident light power. Figure 2c shows the corresponding

photocurrents of the three kesterite photodetectors, plotted as a function of light power (symbols) in a log–log plot. For comparison, the horizontal dashed lines mark the noise floor (measured noise current at 0 V and $f = 733$ Hz; see Figure 1c). Further, the black solid line is a guide to the eye with a slope of one, indicating the linear regime as expected in the absence of higher-order photocurrent loss mechanisms.[27] All three devices show a linear photocurrent-to-light power behavior within the probed intensity window (i.e., 10^{-12} to 10^{-3} W) amounting to a linear dynamic range (LDR) of $\approx$180 dB (nine orders of magnitude). It is expected that higher-order photocurrent loss mechanisms (e.g., second-order, bimolecular recombination, or series resistance limitations) will eventually lead to a deviation from linearity at higher light power ($>10^{-2}$ W).[27]

The NEP$_\lambda$ were estimated to be 3.63×10^{-12} WHz$^{-1/2}$ (30 nm), 2.24×10^{-12} WHz$^{-1/2}$ (50 nm), and 1.09×10^{-12} WHz$^{-1/2}$ (100 nm). Further, NEP$_\lambda$ can be used to evaluate the value of D^* directly through $D_{NEP}^* = \sqrt{A\Delta f}/\text{NEP}_\lambda$. The corresponding D_{NEP}^* for the three CZTS devices at a wavelength of 520 nm were obtained as 1.95×10^{11} Jones (30 nm), 3.16×10^{11} Jones (50 nm),

**ADVANCED
SCIENCE NEWS**

www.advancedsciencenews.com

**ADVANCED
PHOTONICS
RESEARCH**
Open Access

www.adpr-journal.com

Figure 2. a) Specific detectivity, as obtained from spectral responsivity (solid line) and NEP measurements (symbols), plotted as a function of wavelength and compared for CZTS devices with different CdS buffer layer thicknesses. b) Photocurrent response of a 30 nm CdS buffer layer CZTS device plotted against the frequency and compared for different incident light intensities. The 520 nm probe light was modulated at 733 Hz. c) Photocurrent at zero applied bias voltage of all three CZTS devices ($A = 0.5\,cm^2$) plotted as a function of light power. While symbols are experimental data, horizontal dashed lines mark the noise floor; the black solid line is a guide to the eye with a slope of one. d) Normalized (relative) response of all three CZTS photodetectors plotted as a function of input signal frequency. Vertical lines mark the corresponding cut-off frequencies obtained at −3 dB (horizontal line).

and 6.49×10^{11} Jones (100 nm). As shown in Figure 2a, D^*_{NEP} (symbols) and D^*_R (solid lines) are found to be in excellent agreement with each other at this wavelength.

2.3. Frequency Response

Next, we probed the frequency response of the three PDs at zero applied bias voltage. Figure 2d illustrates the photocurrent response (relative to continuous wave illumination) as a function of modulation frequency. Typically, the bandwidth of a photodetector is given in terms of the −3 dB frequency ($f_{-3\,dB}$), defined as the frequency at which the device response has declined by 50% in comparison to continuous wave illumination. As shown in Figure 2d, all three CZTS photodetectors have similar −3 dB frequencies with $f_{-3dB} \approx 25.1\,kHz$ (30 nm), $f_{-3dB} \approx 22.6\,kHz$ (50 nm), and $f_{-3dB} \approx 29.6\,kHz$ (100 nm). We note that the −3 dB cut-off frequency is below the corresponding RC-limited bandwidths (f_{RC}) of around 1 MHz, where $f_{RC} = R_{shunt} \times \varepsilon_{CZTS}\varepsilon_0 A/d$; assuming a dielectric constant for the kesterite CZTS absorber material of $\varepsilon_{CZTS} = 13.7$, an active

layer thickness of $d = 2\,\mu m$, and an pixel area of $A = 0.5\,cm^2$. The origin of the deviation between f_{-3dB} and f_{RC} could be related to various processes: i) the transit or drift motion of photogenerated electrons and holes under the effect of an electric field in the depletion region, ii) the diffusion motion of such carriers under no applied field outside the depletion region, and iii) trapping of carriers at the interface or by defects.

2.4. Dark Current

We next investigated the origin of the relatively high dark currents in the CZTS photodetectors. The corresponding $I_D–V$ curves of all three CZTS devices are shown in **Figure 3**a–c. We also conducted light intensity dependent $I_{sc}–V_{oc}$ measurements (see Experimental Section) to avoid transport- and series resistance limitations present in the dark current at (high) forward bias voltages. In general, the current can be described by the (nonideal) diode equation: $I_D = V/R_{shunt} + I_{diode}(V)$. Here, $I_{diode}(V)$ is the diode current generally being of the form $I_{diode}(V) \propto I_0 \exp(qV/n_{id}k_B T)$ in the forward bias, where I_0 denotes the dark saturation current and n_{id} is the diode ideality factor. While for direct, band-to-band transitions, $n_{id} = 1$, trap-assisted Shockley–Read–Hall (SRH) recombination is expected to lead to n_{id}-values ranging between 1 and 2 (depending on the trap energetics and distribution). In our case, we found that the dark current is well described by an ideality factor close to 2 suggesting that trap-assisted SRH recombination mediated via mid-gap states is playing a major role. To fully account for the effect of trap-mediated transitions, the diode current is described by $I_{diode}(V) = I_{0,2}\eta_{0,2}(V)A[\exp(\frac{qV}{2kT}) - 1]$, which also considers the additional voltage dependence [$\eta_{0,2}(V)$] of the diode current induced by nonuniform carrier distributions in the device.[28] The corresponding model fits (indicated by solid lines) of the $I_D–V$ curves are shown in Figure 3a–c. As shown in Figure 3a–c, at reverse and small forward bias voltages, a good agreement between the experimental $I_D–V$ curves (open square symbols), the $I_{sc}–V_{oc}$ data (closed triangle symbols), and the diode model (black solid lines) are found. From the diode model, we further extracted dark saturation currents of $I_0 \approx 3.67 \times 10^{-8}$ A (30 nm), $I_0 \approx 5.48 \times 10^{-7}$ A (50 nm) and 2.07×10^{-7} A (100 nm). We note that the presence of trap states can also be observed when plotting the photocurrent as a function of light power in a log–log plot (see Figure 2c), where a deviation from linearity may occur at low intensity depending on their distribution and density.[27] However, in our case, we did not observe a deviation from linearity for the three kesterite photodetectors; this is also consistent with what is expected in case of mid-gap state dominated recombination.

2.5. Specific Detectivity Limits

Specific detectivities of three kesterite CZTS photodetectors at zero applied bias voltage were found to slightly increase with increasing CdS buffer layer thickness from D^*_R of 1.91×10^{11} Jones (30 nm), 3.66×10^{11} Jones (50 nm), and 7.12×10^{11} Jones (100 nm) (see **Figure 4**a). To the best of our knowledge, the latter value is one of the highest specific detectivity values reported for kesterite CZTS photodetectors to date.[29] To demonstrate the full potential
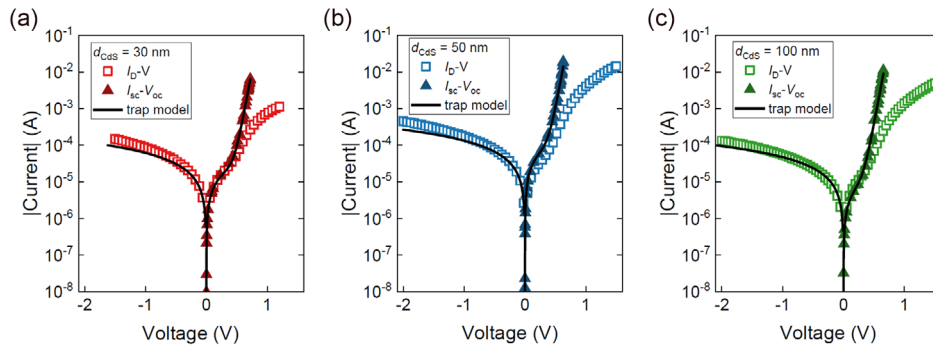
Figure 3. Dark current versus applied voltage (open square symbols), short-circuit current versus open-circuit voltage (closed triangle symbols) and fit to the (nonideal) trap diode model (black solid line) of kesterite CZTS device with CdS buffer layer thickness of a) 30 nm, b) 50 nm, and c) 100 nm.
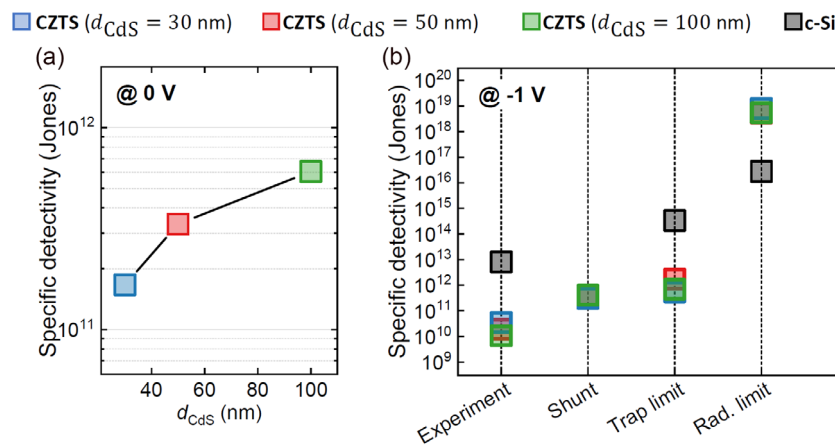
Figure 4. a) Experimentally determined specific detectivity (D_R^*) of kesterite CZTS photodetectors at zero applied bias voltage and compared for different CdS buffer layer thickness. b) Measured specific detectivity of kesterite CZTS photodetectors, as obtained at -1 V applied bias voltage, and compared to various upper limits associated with: i) shunt resistance-induced thermal noise; ii) trap-state diode model-related dark saturation current; and iii) radiative dark saturation current. For comparison, a c-Si photodiode is also shown.

of kesterite-based photodetectors, the upper, radiative limit of specific detectivity of the CZTS devices were determined. To this end, photovoltaic EQE (EQE$_{PV}$) measurements were conducted using our home-built EQE apparatus[30] (see Method section), from which the radiative dark saturation current, $I_{0,rad}$, was calculated via $I_{0,rad} = qA \int_0^\infty EQE_{PV} \varphi_{BB} dE$.[31] Here, E is the photon energy, and φ_{BB} is the black body spectrum. $I_{0,rad}$ was found to be 2.1×10^{-21} A (30 nm), 1.2×10^{-21} A (50 nm), and 1.7×10^{-21} A (100 nm), and was further used to calculate the corresponding radiative limit of specific detectivity according to $D_{rad}^* = R_\lambda \sqrt{A} / \sqrt{2qI_{0,rad}}$. For comparison, a crystalline silicon (c-Si) (a representative of a typical inorganic semiconductor photodetector operating in a similar VIS spectral window as the kesterite CZTS devices studied in this work) was added.

Figure 4b shows D_{rad}^* of the three kesterite photodetectors compared with the c-Si reference device. As expected, due to the low bandgap of c-Si ($E_{g,c-Si} \approx 1.1$ eV), as compared to the kesterite devices studied in this work ($E_{g,kesterite} \approx 1.4$ eV), D_{rad}^* of c-Si is approximately three orders of magnitude smaller than those of the CZTS kesterite photodetectors. For comparison, the

corresponding experimental D_R^* at a reverse bias of -1 V (where the noise current is not dominated by the thermal noise from R_{shunt}) are included in Figure 4b. The relative reductions in D_R^* compared to D_{rad}^*, associated with nonradiative (NR) losses, in the three kesterite devices were found to be roughly 6 orders of magnitude, i.e., much larger compared to the c-Si reference device.

The higher NR losses in the CZTS devices are also reflected in the corresponding NR loss analysis determined based on the EQE$_{PV}$ and the measured V_{oc} under artificial 1 sun ($V_{oc,exp}$) via $\Delta V_{NR} = V_{oc,rad} - V_{oc,exp}$. Here, $V_{oc,rad}$ is the radiative V_{oc} limit given by $V_{oc,rad} = (k_B T/q) \ln [I_{ph}/I_{0,rad} + 1]$, where I_{ph} is the expected photocurrent under 1 sun illumination, $I_{ph} = qA \int_0^\infty EQE_{PV} \varphi_{sun} dE$ (φ_{sun} is the solar spectrum). Based on this, we observe CZTS devices to show a roughly three times higher ΔV_{NR} [$\Delta V_{NR} \approx 0.466$ V (30 nm), $\Delta V_{NR} \approx 473$ V (50 nm), and $\Delta V_{NR} \approx 0.464$ V (100 nm)] compared to c-Si ($\Delta V_{NR} \approx 0.2$ V), which is in agreement with the higher D_R^* of c-Si.

The observation that the ideality factor in all three CZTS devices is close to 2 (see fits to I_D-V curves in Figure 3) suggests that the

2300177 (5 of 7)

**ADVANCED
SCIENCE NEWS**

www.advancedsciencenews.com

**ADVANCED
PHOTONICS
RESEARCH**

www.adpr-journal.com

NR losses are (partially) caused by defect states. The corresponding I_0 represents the upper limit of the dark saturation current for the case that the NR transitions occur solely via mid-gap traps. The extracted $I_{0,2}$ values were used to calculate the corresponding diode specific detectivity (trap) limits (Figure 4b) at -1 V, which were found to be two orders of magnitude higher compared to the experimentally obtained D_R^*. However, these values are only marginally higher than the specific detectivity limits, expected based on the thermal noise from the shunt resistances (see Figure 4b), which dominate the noise current at 0 V. Subsequently, both trap-mediated recombination in the bulk and thermal noise from the shunt alone cannot fully account for the observed NR losses in the CZTS devices, implying that additional loss channels are present. This is also observed in the comparison between the experimentally obtained V_{oc} under 1 sun and the theoretical, mid-gap trap state-dominated would-be V_{oc}, $V_{oc,n_{id}=2}$, as obtained from $I_{0,2}$ (trap diode model) via $V_{oc,n_{id}=2} = (2k_BT/q)\ln(I_{sc}/I_{0,2})$. Here, $V_{oc,n_{id}=2} \neq V_{oc}$ is observed for all three kesterite CZTS devices, confirming the presence of additional NR loss channels. Our experimental data further suggest that these additional losses vary with buffer layer thickness (being the lowest for the 50 nm thick CdS kesterite photodetector when probed at -1 V). These additional losses can be assigned to interface recombination induced by unoptimized conduction band alignment at the kesterite/CdS interface, which has previously been found to limit the V_{oc} under 1 sun conditions.[32]

3. Conclusion

In conclusion, the impact of the CdS buffer layer thickness on the performance metrics in kesterite CZTS photodetectors was investigated. In this regard, we have characterized the CZTS devices with respect to their noise current, spectral responsivity, NEP, frequency response, and specific detectivity. We found high shunt currents and defect-induced nonradiative losses to primarily limit the CZTS photodetector performance; relative comparisons between various detectivity limits, however, suggest the presence of additional, CdS buffer layer-related loss channels. The experimentally obtained specific detectivity at short circuit was found to be maximum for the 100 nm CdS layer thick CZTS performing best with approximately 7.12×10^{11} Jones. From photovoltaic EQE measurements, the upper radiative limit of specific detectivity for all three CZTS devices was estimated to amount to approximately 10^{19} Jones. This clearly shows the potential of kesterites to be used as a viable, CRM-free candidate for sustainable, environment-friendly PV technology. However, optimization of (CdS) buffer layer, reduction of defect-inducing nonradiative losses, increasing shunt resistances, and careful identification of additional loss channels (e.g., kesterite/buffer layer interface recombination) are needed to push the kesterite photodetector performances closer to their expected limits.

4. Experimental Section

Device Fabrication: The composition of the CZTS absorber used was Cu/Sn 1.94, Zn/(Cu + Sn) 0.4, and Cu/(Zn + Sn) 0.89. They were all deposited in the same sputtering run but annealed under the same conditions in three different annealing runs (in a graphite box with 20 mg added elemental sulfur), at 560 °C for 10 min dwell time as described in [ref. [33]]. After that, the absorber was etched in 5 wt% KCN solution before CdS chemical bath deposition using our baseline recipe but for different times. Top layers were sputtered ZnO and ZnO:Al and top grid Ni/Al/Ni shading 2.5% of the area. The substrate was soda-lime glass with sputtered Mo, around 300 nm thick. All devices had an active area of $A = 0.5$ cm^2.

Light Current Versus Voltage: Current versus voltage characteristics were measured under artificial 1 sun illumination in a Newport ABA solar simulator with short-circuit current density (J_{sc}) calibrated from EQE measurements.

Dark Current Versus Voltage: Dark current versus voltage (I_D–V) characteristics were measured with a Keithley 2450 source meter unit. The device under test (DUT) was mounted in an electrically shielded Linkam sample holder.

Responsivity and External Quantum Efficiency: Responsivity (R) and photovoltaic EQE (EQE$_{PV}$) measurements were performed using a home-built apparatus including a Perkin Elmer UV/VIS/NIR spectrometer (LAMBDA 950) as a source of monochromatic light. The probe light was physically chopped at 273 Hz and directed onto the DUT. The resulting photocurrent was amplified by a low-noise current preamplifier (FEMTO DLPCA-200) and measured with a Stanford SR860 lock-in amplifier. The DUT was mounted in an electrically shielded Linkam sample holder. For calibration, a NIST-calibrated silicon (818-UV, Newport) and germanium (818-IR, Newport) photodiode were used as reference devices. A detailed description of the apparatus is provided elsewhere.[30]

Noise Current and Linear Dynamic Range (LDR): The noise current measurements were performed in the dark using a Linkam sample holder to avoid electrical pick-up noise. The noise current of the DUT was amplified using a Stanford SR570 low-noise current preamplifier and measured with a Keysight N9010B Signal Analyzer with the resolution bandwidth set to 1 Hz over a frequency range of 10 Hz to 1 kHz. The same setup was used to measure the linear dynamic range, except for the DUT being illuminated by a 520 nm laser source (Oxxius L6Cc laser) modulated by a Keysight 33600 A series waveform generator at 733 Hz. To record the frequency response over light powers spanning ten orders of magnitude, the light power was controlled via the pump current that drives the laser and additional ND-filters (Thorlabs).

Short-Circuit Current Versus Applied Voltage: A 520 nm customized CW laser modulated at low frequency (i.e., < 0.1 Hz) was used for short-circuit current versus open-circuit voltage (I_{sc}–V_{oc}) measurements conducted in air. The DUT was mounted in an electrically shielded Linkam sample holder. A motorized two-wheel attenuator from Standa (10MCWA168-1) containing different optical density filters was used for gradual light intensity attenuation. The I_{sc} and V_{oc} of the DUT were recorded with a Keithley 2450 source meter unit. Detailed information to the I_{sc}–V_{oc} are provided elsewhere.[27,34]

Conflict of Interest

The authors declare no conflict of interest.

Data Availability Statement

The data that support the findings of this study are available from the corresponding authors upon reasonable request.

Keywords

[1] K. S. Gour, V. Karade, P. Babar, J. Park, D. M. Lee, V. N. Singh, J. H. Kim, *Solar RRL* **2021**, *5*, 2000815.

[2] A. S. Nazligul, M. Wang, K. L. Choy, *Sustainability* **2020**, *12*, 5138.

[3] S. Chen, A. Walsh, J. H. Yang, X. G. Gong, L. Sun, P. X. Yang, J. H. Chu, S. H. Wei, *Phys. Rev. B* **2011**, *83*, 125201.

[4] M. Grossberg, J. Krustok, C. J. Hages, D. M. Bishop, O. Gunawan, R. Scheer, S. M. Lyam, H. Hempel, S. Levcenco, T. Unold, *J. Phys. Energy* **2019**, *1*, 044002.

[5] J. S. Seol, S. Y. Lee, J. C. Lee, H. D. Nam, K. H. Kim, *Sol. Energy Mater. Sol. Cells* **2003**, *75*, 155.

[6] Y. Gong, Q. Zhu, B. Li, S. Wang, B. Duan, L. Lou, C. Xiang, E. Jedlicka, R. Giridharagopal, Y. Zhou, Q. Dai, W. Yan, S. Chen, Q. Meng, H. Xin, *Nat. Energy* **2022**, *7*, 966.

[7] W. Wang, M. T. Winkler, O. Gunawan, T. Gokmen, T. K. Todorov, Y. Zhu, D. B. Mitzi, *Adv. Energy Mater.* **2013**, *4*, 1301465.

[8] H. Kyung Park, Y. Cho, J. Kim, S. Kim, S. Kim, J. Kim, K.-J. Yang, D.-H. Kim, J.-K. Kang, W. Jo, *NPJ Flex. Electron.* **2022**, *6*, 91.

[9] A. Apostolopoulou, S. Mahajan, R. Sharma, E. Stathatos, *J. Phys. Chem. Solids* **2018**, *112*, 37.

[10] Z. Hou, Y. Li, J. Liu, H. Shen, X. Huo, *New J. Chem.* **2021**, *45*, 1743.

[11] N. M. Shinde, P. R. Deshmukh, S. v. Patil, C. D. Lokhande, *Sens. Actuators A, Phys.* **2013**, *193*, 79.

[12] K. v. Gurav, S. W. Shin, U. M. Patil, P. R. Deshmukh, M. P. Suryawanshi, G. L. Agawane, S. M. Pawar, P. S. Patil, J. Y. Lee, C. D. Lokhande, J. H. Kim, *Sens. Actuators B, Chem.* **2014**, *190*, 408.

[13] K. S. Gour, O. P. Singh, B. Bhattacharyya, R. Parmar, S. Husale, T. D. Senguttuvan, V. N. Singh, *J. Alloys Compd.* **2017**, *694*, 119.

[14] M. Azzouzi, A. Cabas-Vidani, S. G. Haass, J. A. Röhr, Y. E. Romanyuk, A. N. Tiwari, J. Nelson, *J. Phys. Chem. Lett.* **2019**, *10*, 2829.

[15] A. Redinger, T. Unold, *Sci. Rep.* **2018**, *8*, 1874.

[16] H. Sharif, T. Enkhbat, E. Enkhbayar, J. Kim, *ACS Appl. Energy Mater.* **2020**, *3*, 8500.

[17] A. Wang, M. He, M. A. Green, K. Sun, X. Hao, *Adv. Energy Mater.* **2023**, *13*, 2203046.

[18] S. Chen, A. Walsh, X.-G. Gong, S.-H. Wei, S. Chen, S.-H. Wei, X.-G. Gong, A. Walsh, *Adv. Mater.* **2013**, *25*, 1522.

[19] A. Pu, F. Ma, C. Yan, J. Huang, K. Sun, M. Green, X. Hao, *Sol. Energy Mater. Sol. Cells* **2017**, *160*, 372.

[20] L. Grenet, F. Emieux, J. Andrade-Arvizu, E. de Vito, G. G. Lorin, Y. Sánchezsánchez, E. Saucedo, F. Frédé, F. Roux, *ACS Appl. Energy Mater.* **2020**, *3*, 1883.

[21] C. Platzer-Björkman, N. Barreau, M. Bär, L. Choubrac, L. Grenet, J. Heo, T. Kubart, A. Mittiga, Y. Sanchez, J. Scragg, S. Sinha, M. Valentini, *J. Phys.: Energy* **2019**, *1*, 44005.

[22] M. He, C. Yan, J. Li, M. P. Suryawanshi, J. Kim, M. A. Green, X. Hao, *Adv. Sci.* **2021**, *8*, 2004313.

[23] J. Zhou, X. Xu, H. Wu, J. Wang, L. Lou, K. Yin, Y. Gong, J. Shi, Y. Luo, D. Li, H. Xin, Q. Meng, *Nat. Energy* **2023**, *8*, 526.

[24] O. P. Singh, A. Sharma, K. S. Gour, S. Husale, V. N. Singh, *Sol. Energy Mater. Sol. Cells* **2016**, *157*, 28.

[25] K. S. Gour, B. Bhattacharyya, O. P. Singh, A. K. Yadav, S. Husale, V. N. Singh, *J. Alloys Compd.* **2018**, *735*, 285.

[26] W. Li, D. Xiong, M. Xie, C. Luo, X. Zeng, Y. Gao, B. Guo, C. Yan, F. Chun, Z. Zhu, X. Fan, W. Deng, W. Yang, *J. Mater. Chem. C* **2020**, *8*, 3491.

[27] S. Zeiske, W. Li, P. Meredith, A. Armin, O. J. Sandberg, *Cell Rep. Phys. Sci.* **2022**, *3*, 101096.

[28] O. J. Sandberg, C. Kaiser, S. Zeiske, N. Zarrabi, S. Gielen, W. Maes, K. Vandewal, P. Meredith, A. Armin, *Nat. Photonics* **2023**, *17*, 368.

[29] H. Wu, C. Ma, J. Zhang, H. Cao, R. Lin, W. Bai, Z. Pan, J. Yang, Y. Zhang, Y. Chen, X. Tang, X. Wang, J. Wang, J. Chu, *ACS Appl. Electron. Mater.* **2021**, *3*, 4135.

[30] S. Zeiske, C. Kaiser, P. Meredith, A. Armin, *ACS Photonics* **2019**, *7*, 256.

[31] U. Rau, *Phys. Rev. B* **2007**, *76*, 085303.

[32] T. Ericson, F. Larsson, T. Törndahl, C. Frisk, J. Larsen, V. Kosyak, C. Hägglund, S. Li, C. Platzer-Björkman, *Solar RRL* **2017**, *1*, 1700001.

[33] T. Ericson, J. J. Scragg, A. Hultqvist, J. T. Watjen, P. Szaniawski, T. Torndahl, C. Platzer-Bjorkman, *IEEE J. Photovolt.* **2014**, *4*, 465.

[34] S. Zeiske, O. J. Sandberg, N. Zarrabi, W. Li, P. Meredith, A. Armin, *Nat. Commun.* **2021**, *12*, 3603.